A Generalized Geodesic Voting Framework for Interactive Image Segmentation

Shuwang Zhou, Li Liu, Da Chen, Hui Liu, Laurent D. Cohen, Minglei Shu

A Generalized Geodesic Voting Framework for Interactive Image Segmentation

Shuwang Zhou, Li Liu, Da Chen, Hui Liu, Laurent D. Cohen, *Fellow, IEEE*, and Minglei Shu

***Abstract*—In this paper, we introduce a novel interactive image segmentation method based on the geodesic voting formulation. In contrast to the classical geodesic voting model which utilizes the geodesics only depending on the path position, the proposed model also takes into account the image edge anisotropic and asymmetric features by adapting the minimal paths relying on the asymmetric quadratic metric for geodesic voting. Furthermore, an adaptive cut-based closed contour computation scheme is invoked to depict the target boundary, by tracing two asymmetric minimal paths from a source point located at the adaptive cut to an end point along two opposite sides of the cut. The proposed asymmetric geodesic voting model is then applied to get the complex structure segmentation, benefiting from the asymmetric features and cut-convexity constraint. Experimental results show that the proposed model indeed outperforms state-of-the-art minimal paths-based image segmentation approaches.**

***Index Terms*—geodesic voting, image segmentation, feature extraction, geodesic models, Hamilton-Jacobi-Bellman equation.**

I. Introduction

Image segmentation is a fundamental task in the fields of computer vision, medical imaging and engineering, yielding a broad variety of efficient and practical solutions. In particular in the field of instrument and measurement, the segmentation procedure, whose basic goal is to divide the image domain into a series of subregions, is known as an important post-processing step to achieve the measurement task. In this paper, we focus on the variational models, among which the benefits from image features and geometric regularization can be naturally integrated for extracting image boundaries of interests.

Among the existing variational segmentation models, the active contour approaches have been widely studied since the original work [1] and have been inspired a great number of successful applications [2]–[5] in image analysis and computer vision. The geodesic active contour model [6], [7] is a reliable model for image segmentation, which can blend the benefits from both geometry of the contours and the local image gradient features, relying on a level set scheme [8]. Image gradients are simple and efficient features in defining object boundaries, but sensitive to image noise and spurious edges. Region-based active contour models are regarded as a powerful solution to the problems encountered by the edge-based models. In the region-based models, image features such as colors and gray levels can be modeled using statistical models, where typical examples of relevant approaches include [9]–[11].

However, the level set-based active contour models are prone to trap into local minima, whose numerical solutions are sensitive to parameters, thus preventing their practical applications in image analysis and artificial intelligence. In order to tackle the issue, Cohen and Kimmel proposed a minimal geodesic model that globally minimizing weighted curve length [12] associated to an direction-independent Riemannian metric, by simply specifying two endpoints at the target curve. Using the eikonal equation framework, the problem of finding minimal geodesic paths is naturally transferred to the computation of a geodesic action map, which carries the minimization of the weighted length. The efficiency is guaranteed by the fast marching method [13], [14], known as a very numerical solution to the Hamilton–Jacobi–Bellman (HJB) equation.

Geodesic Paths-based Image Segmentation Models. The geodesic models have been extensively used in image segmentation task, due to their computation efficiency and global optimality. A crucial point for geodesic-based segmentation approaches is to model the object boundaries as a simple closed curves consisting of geodesic paths. In [12], a saddle point detection method is introduced for finding two minimal paths from a single source point, whose combination is a simple closed curve, thus solving the image segmentation problem. In [17], Mille *et al*. extended this idea to the case of extracting multiple minimal paths from a set of saddle points, allowing to incorporate a set of user-provided landmark points for interactive segmentation. In contrast to the models which delineate a complete object boundary using a set of open geodesic paths, the circular geodesic model [18] proposed to find a simple and closed planar geodesic, implemented by introducing a cut as a straight segment whose two sides are supposed to be disconnected. However, this model requires external procedure to ensure the simplicity of the circular geodesic, especially when the target region has a complicated shape. Chen *et al.* introduce a dual-cut scheme [16] to construct a simple closed curve consisting of two disjoint minimal paths. Recent works on geodesic models allow to

Shuwang Zhou is with College of Computer Science and Engineering, Shandong University of Science and Technology, Qingdao, 266590, China. He is also with Shandong Artificial Intelligence Institute, Qilu University of Technology (Shandong Academy of Sciences), Jinan, 250014, China (e-mail: zhoushw@sdas.org)

Li Liu is with Department of Rehabilitation Medicine, Tong Ren Hospital, Shanghai Jiao Tong University School of Medicine, 200336, Shanghai, China. She is also with Institute of Rehabilitation, Shanghai Jiao Tong University School of Medicine, 200025, Shanghai, China. (e-mail: liuli19910101@163.com)

Laurent D. Cohen is with University Paris Dauphine, PSL Research University, CNRS, UMR 7534, CEREMADE, 75016 Paris, France.

Da Chen, Hui Liu and Minglei Shu are with Shandong Artificial Intelligence Institute, Qilu University of Technology (Shandong Academy of Sciences), Jinan, 250014, China (e-mail: shuml@sdas.org).

Corresponding authors: Li Liu and Minglei Shu.

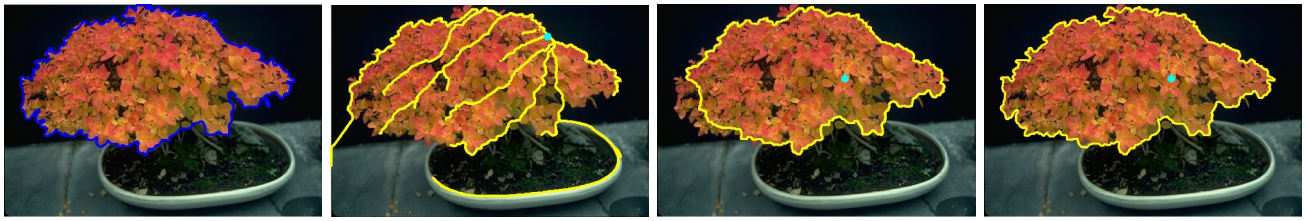

(a) (b) (c) (d)

Fig. 1. An example for visualizing the advantages of the proposed generalized geodesic voting model. **a** An original image, where the blue line indicates the ground truth. **b** Segmentation results denoted by yellow lines from the classic geodesic voting segmentation model [15], the dual-cut model [16] and the proposed geodesic voting model featuring asymmetry enhancement, respectively. The cyan points in (c) and (d) depict the landmark points.

take into account the region-based statistical features [19] and curvature regularization [20]–[23] for image segmentation, yielding promising segmentation results.

Minimal paths are very often used as a fundamental tool for extracting image features through a voting manner [24]. A key ingredient of the geodesic voting method lies at the use of a set of sampled points, each of which leads to a minimal path linking to the fixed source point, thus regarded as an endpoint of the path. These sampled points are produced being such that they are distributed densely around the features of interest, thus encouraging the voting method to detect as much image features relevant to the user intervention as possible. In contrast to the circular path models or saddle points-based models which take only a single closed curve as the segmentation contour, the geodesic voting method can benefit from the statistical information of a large amount of minimal paths. Such an advantage allows the geodesic voting model to correctly find the expected segmentation contours, even through the images have complex intensity distributions. Furthermore, the geodesic voting method is originally applied for tubular structure tracking [24], [25], where the target features (i.e. tubular tree structure) can be modeled as a series of open minimal paths associated to Riemannian type of metrics. In [15], the authors investigated the geodesic voting method for edge detection and image segmentation. Unfortunately, these geodesic voting models fail to take advantages of the directional property of closed curves to create the set of voting paths. Moreover, these models utilize all the voting paths to compute a voting score map, which may increase the probability of generating spurious edges. Considering the above two issues suffered by the classical geodesic voting method, we propose a new geodesic voting method consisting of asymmetric quadratic metrics and two voting paths selection criteria. As a consequence, the directional property of segmentation contours can be fully used.

Existing geodesic voting models fall into the limitation that only the Riemannian metrics are invoked to compute the voting paths. In particular, the image gradients are known as an important cue that reflects the directions of the target edges. However, minimal paths associated with the type of Riemannian metrics fails to make use of the full information of the image gradient features, due to its symmetric nature with respect to the path tangents. We show an example of comparison of different minimal paths-based segmentation models on a real image, as shown in Fig. 2a where the blue line indicates the expected segmentation contour. Fig. 2b illustrates the results from the classical geodesic voting method, which appears as a set of open curves, thus failing to find the correct segmentation contour. Fig. 2c gives the segmentation contour of the dual-cut model that is a variant of the circular geodesic model. One can point out that a part of the target boundary is missed due to its weak edge appearance. Fig. 2d illustrates the segmentation contour derived from the proposed geodesic voting method, which is able to correctly capture the target boundary.

In addition, deep learning technique has obtained great success in various image segmentation tasks as reviewed in the literature [26], [27], thanks to the powerful ability of data fitting carried out via the neural network. Significant deep learning-driven segmentation approaches include [28]–[35], which have inspired a variety of research lines to address various image segmentation problems. As a great advantage, the benefits from both of the high level image features (e.g. the semantic information) and the low level features can be blended into the these models. However, despite their great advances, the deep learning-based segmentation models commonly lack the regularization derived from the weighted curve length associated to Finslerian metrics. In practical applications, this often yields unexpected segmentation contours which are not smooth, especially for medical images where the target boundaries often suffer from unexpected interruption. In contrast, the proposed method that integrates geometric regularization (e.g. the weighted curve length invoked in this paper) is able to alleviate this problem.

In this work, we introduce a new geodesic voting method in conjunction with an adaptive cut for interactive image segmentation. Our contributions are twofold.

- Firstly, we consider an asymmetric quadratic metric to compute the voting paths. This allows to benefit from the directional features which are asymmetric with to path tangents. As a result, the full image gradient features are taken into account.
- Secondly, a new geodesic voting method including the incorporation of an adaptive cut and two voting path selection criteria is introduced. This allows the model to choose more relevant voting paths to build the final voting score map, thus encouraging to find more accurate segmentation results when comparing to the traditional minimal paths-based models.

This paper is organized as follows. The basic formulation of the adaptive geodesic voting scheme and general minimal path model can be reviewed in Section II. The main contribution of this paper, i.e. a generalization of the asymmetric geodesic voting scheme for image segmentation applications, is detailed in Section III. The experimental results and the conclusion are formulated in Sections IV and V, respectively.

II. Background

A. Background on the General Minimal Path Model

We start by introducing some basic mathematical notations of the geodesic model. Let $\mathbb{M} \subset \mathbb{R}^2$ be an open and bounded domain. We further denote by $\mathrm{Lip}([0,1],\mathbb{M})$ the set of all Lipschitz continuous curves $\gamma : [0,1] \to \mathbb{M}$ which is regarded as the search space of minimal paths.

Different from the isotropic manner, the general minimal path model measures the weighted length of regular curves not only depending on the local curve position but also its orientation, by utilizing an anisotropic and asymmetric Finsler metric [7]. The weighted length of a curve $\gamma \in \mathrm{Lip}([0,1],\mathbb{M})$ associated to a general Finsler metric $\mathcal{F} : \mathbb{M} \times \mathbb{R}^2 \to [0,+\infty]$ can be computed by

$$\mathcal{L}_{\mathcal{F}}(\gamma) = \int_0^1 \mathcal{F}(\gamma(t), \gamma'(t))dt. \tag{1}$$

Similar to the original case, the distance $\ell_{\mathcal{F}}(\mathbf{x},\mathbf{y})$ for two points $\mathbf{x},\mathbf{y} \in \mathbb{M}$ can be obtained by globally minimizing the weighted curve length associated to the Finsler metric $\mathcal{F}$ as

$$\ell_{\mathcal{F}}(\mathbf{x},\mathbf{y}) = \inf_{\gamma \in \mathrm{Lip}([0,1],\mathbb{M})} \{\mathcal{L}_{\mathcal{F}}(\gamma); \gamma(0) = \mathbf{x}, \gamma(1) = \mathbf{y}\}. \tag{2}$$

Given a source point $\mathbf{s} \in \mathbb{M}$ and a target point $\mathbf{x} \in \mathbb{M}$, the value of $\mathcal{U}_{\mathbf{s}}(\mathbf{x})$ corresponding to the geodesic distance map $\mathcal{U}_{\mathbf{s}} : \mathbb{M} \to [0,\infty)$ can be computed as

$$\mathcal{U}_{\mathbf{s}}(\mathbf{x}) = \ell_{\mathcal{F}}(\mathbf{s},\mathbf{x}), \forall \mathbf{x} \in \mathbb{M}\backslash\{\mathbf{s}\}. \tag{3}$$

Then, a minimal path $\mathcal{G}_{\mathbf{s},\mathbf{x}} \in \mathrm{Lip}([0,1],\mathbb{M})$ with $\mathcal{G}_{\mathbf{s},\mathbf{x}}(0) = \mathbf{s}$ and $\mathcal{G}_{\mathbf{s},\mathbf{x}}(1) = \mathbf{x}$ can be tracked on the distance map as

$$\mathcal{G}_{\mathbf{s},\mathbf{x}} = \arg\min_{\gamma \in \mathrm{Lip}([0,1],\mathbb{M})} \{\mathcal{L}_{\mathcal{F}}(\gamma); \gamma(0) = \mathbf{s}, \gamma(1) = \mathbf{x}\}. \tag{4}$$

The geodesic distance map $\mathcal{U}_{\mathbf{s}} : \mathbb{M} \to [0,\infty)$ can be estimated by solving the first-order static HJB equation [14], [36]

$$\begin{cases} \mathcal{H}_{\mathbf{x}}(\nabla \mathcal{U}_{\mathbf{s}}(\mathbf{x})) = 1/2, \quad \forall \mathbf{x} \in \mathbb{M}\backslash\{\mathbf{s}\}, \\ \mathcal{U}_{\mathbf{s}}(\mathbf{s}) = 0, \end{cases} \tag{5}$$

where $\mathcal{H}$ is the Hamiltonian of the metric $\mathcal{F}$.

Then the target minimal path $\mathcal{G}_{\mathbf{s},\mathbf{x}} \in \mathrm{Lip}([0,1],\mathbb{M})$ can be computed in terms of the geodesic flows

$$\mathbf{V}(\mathbf{x}) = d\mathcal{H}_{\mathbf{x}}(\nabla \mathcal{U}_{\mathbf{s}}(\mathbf{x})), \tag{6}$$

leading to the following original differential equation (ODE) [36], [37] for tracking a minimal path $\tilde{\mathcal{G}}_{\mathbf{x},\mathbf{s}}$ as

$$\tilde{\mathcal{G}}'_{\mathbf{x},\mathbf{s}}(t) = -\mathbf{V}(\tilde{\mathcal{G}}_{\mathbf{x},\mathbf{s}}(t)), \tag{7}$$

with $\tilde{\mathcal{G}}_{\mathbf{x},\mathbf{s}}(0) = \mathbf{x}$ and $\tilde{\mathcal{G}}_{\mathbf{x},\mathbf{s}}(1) = \mathbf{s}$. Finally, we can re-parameterize $\tilde{\mathcal{G}}_{\mathbf{x},\mathbf{s}}$ to generate a geodesic curve $\mathcal{G}_{\mathbf{s},\mathbf{x}} \in \mathrm{Lip}([0,1],\mathbb{M})$ obeying $\mathcal{G}_{\mathbf{s},\mathbf{x}}(0) = \mathbf{s}$ and $\mathcal{G}_{\mathbf{s},\mathbf{x}}(1) = \mathbf{x}$.

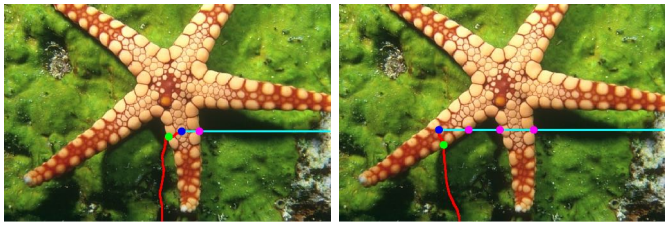

Fig. 2. An example for visualizing the difference between the axis cut and the adaptive cut. The axis cut [18] and adaptive cut [38] are represented by the cyan and red lines. The blue points are the landmark points inside the target region. The magenta (resp. greed) dots are the interaction points between the target contour and the axis cuts (resp. adaptive cuts).

B. Asymmetric Quadratic Metrics

Typical instances of Finsler metrics involve the Randers metrics [19], [39] and the asymmetric quadratic metrics [21], [40]. In this work, we utilize a Finsler metric with an asymmetric quadratic form, which is asymmetric with its second argument. The image edge asymmetry features can be taken into account for estimating the anisotropic and asymmetric minimal paths. In the remaining of this subsection, we will briefly review the asymmetric quadratic metric. Let $\mathbb{S}_2^+$ denote a set collecting all the positive definite symmetric matrices with size of 2×2. The asymmetric quadratic metric $\mathcal{F} := \mathcal{F}_{\mathrm{AQ}}$ is defined as

$$\mathcal{F}_{\mathrm{AQ}}(\mathbf{x},\mathbf{u}) = \sqrt{\langle \mathbf{u}, \mathcal{M}(\mathbf{x})\mathbf{u}\rangle + \langle \omega(\mathbf{x}), \mathbf{u}\rangle_+^2} \tag{8}$$

where $\mathcal{M} : \mathbb{M} \to \mathbb{S}_2^+$ is a tensor field, $\omega : \mathbb{M} \to \mathbb{R}^2$ is a vector field, $\langle \mathbf{u},\mathbf{v}\rangle_+^2 = (\max\{0, \langle \mathbf{u},\mathbf{v}\rangle\})^2$ with $\mathbf{u},\mathbf{v} \in \mathbb{R}^2$. Note that the asymmetric quadratic metric $\mathcal{F}_{\mathrm{AQ}}$ gets to be a Riemannian metric as $\mathcal{F}_{\mathrm{SR}} = \sqrt{\langle \mathbf{u}, \mathcal{M}(\mathbf{x})\mathbf{u}\rangle}$, when the vector field $\omega \equiv 0$. The construction of the metric $\mathcal{F}_{\mathrm{AQ}}$ is based on the image gradient features (See Section B), encoding both the edge appearance and anisotropy information [16].

The tensor field $\mathcal{M}$ is constructed based on the matrix $\mathcal{W}$ in Eq. (25). Let $\vartheta_k(\mathbf{x}) \in \mathbb{R}^2$ with $k = 1,2$ denote the eigenvectors of $\mathcal{W}(\mathbf{x})$. Among them, the eigenvector corresponding to the smaller eigenvalue, referred to as $\vartheta_1(\mathbf{x})$, is perpendicular to the edge tangent of an edge point $\mathbf{x}$. Thus, the eigenvector $\vartheta_2(\mathbf{x})$ can be utilized to indicate the edge anisotropic feature. The tensor field $\mathcal{M}$ can be formulated as

$$\mathcal{M}(\mathbf{x}) = \sum_{k=1}^{2} \exp(a_k g(\mathbf{x})) \vartheta_k(\mathbf{x}) \vartheta_k(\mathbf{x})^T, \tag{9}$$

where the parameter $a_k \in \mathbb{R}$ dominates the anisotropy of the tensor field. In this work, we set $a_1 = 0$ and $a_2 < 0$ for the construction of the anisotropic tensor $\mathcal{M}(\mathbf{x})$.

For constructing the second term ω of the metric $\mathcal{F}_{\mathrm{AQ}}$, a vector field $\varpi : \mathbb{M} \to \mathbb{R}^2$, denoting the edge asymmetry features, is carried out by the gradients of the Gaussian smoothed images, reading as

$$\varpi(\mathbf{x}) = \frac{1}{3} \sum_{m=1}^{3} (\nabla G_\sigma * I_m)(\mathbf{x}). \tag{10}$$

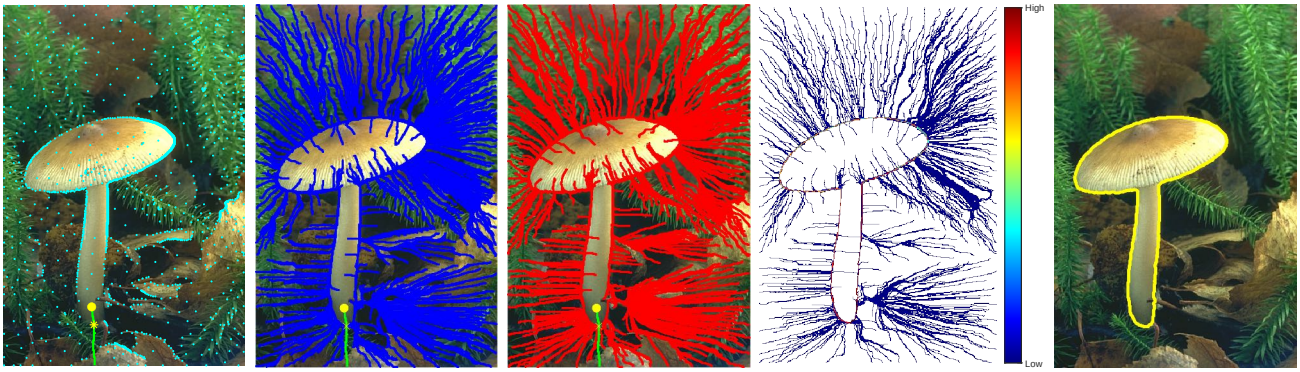

(a) (b) (c) (d) (e)

Fig. 3. Overview of the proposed generalized geodesic voting framework. **a** An original image, where the cyan dots represent the sampled farthest points, the yellow dot depicts the user-provided landmark point $\mathbf{z}$, the green line denotes the adaptive cut and the yellow star indicates the source point $\mathbf{s}$. **b** and **c** Minimal paths which are tracked using the two asymmetric metrics. **e** The visualization of the voting score map. (**f**) The yellow line is the final segmentation contour.

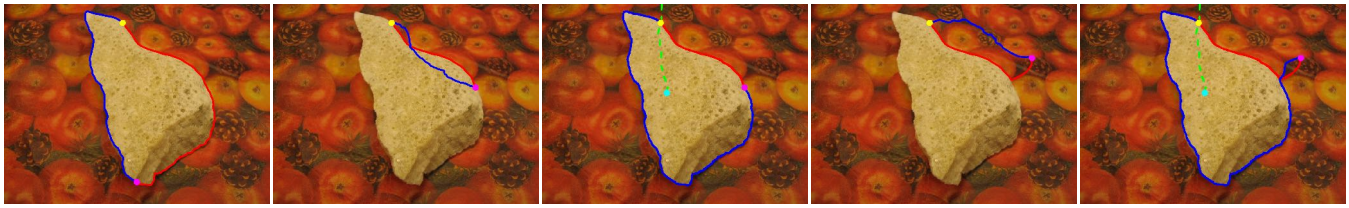

(a) (b) (c) (d) (e)

Fig. 4. Examples of minimal paths associated to asymmetric quadratic metric for boundary detection. The yellow and magenta dots are respectively the source points and endpoints of the minimal paths. **a** Two minimal paths form a simple closed contour, since their source points and endpoints are distributed evenly at the target boundary. **b** and **d** Minimal paths associated to source points and endpoints which are close to each other, where the blue lines suffer from a shortcut problem. **c** and **e** Minimal Paths in conjunction with adaptive cuts (green dash lines), where the yellow dots are the source points $\mathbf{s}$ lying in the adaptive cuts.

The vector $\varpi(\mathbf{x})$ is perpendicular to the edge direction for an edge point $\mathbf{x}$. With this definition, the vector field $\omega := \omega_i$ can be generated by

$$\omega_i(\mathbf{x}) = \begin{cases} \lambda \mathfrak{M}_i \varpi(\mathbf{x}) / \parallel \varpi(\mathbf{x}) \parallel, & \text{if } \parallel \varpi(\mathbf{x}) \parallel \neq 0 \\ 0, & \text{otherwise,} \end{cases} \tag{11}$$

where $\lambda \in \mathbb{R}$ is a scalar parameter, $\mathfrak{M}_i$ denotes the rotation matrix and the corresponding index $i \in \{0, 1\}$ represents the rotation direction of the matrix. In details, $\mathfrak{M}_0$ and $\mathfrak{M}_1$ mean the counter-clockwise and clockwise rotation matrix with rotation angle $\pi/2$, respectively.

C. Geodesic Voting Method

The classical geodesic voting method [24] was firstly introduced for extracting image features. The basic idea is to establish a voting score map $\mathcal{V} : \mathbb{M} \to [0, \infty)$, which is a scalar-valued function, to model the image features of interest. More specifically, this voting score map is generated using a collection of geodesic curves, denoted by $\Phi = \{\mathcal{G}_j\}_{1 \leq j \leq J} \subset \mathrm{Lip}([0, 1], \mathbb{M})$, where J is a positive integer. In general, these geodesic curves for voting score $\mathcal{V}$ are supposed to share the same source point, i.e. $\mathcal{G}_i(0) = \mathcal{G}_k(0), \forall i \neq k$. In this case, the voting score map $\mathcal{V}_{\mathbf{s}}$ reads as [24]

$$\mathcal{V}_{\mathbf{s}}(\mathbf{x}) = \sum_{\mathcal{G} \in \Phi} \chi_{\mathbf{x}}(\mathcal{G}),$$

where $\chi_{\mathbf{x}} : \mathrm{Lip}([0, 1], \Omega) \to \{0, 1\}$ is a detector defined being such that

$$\chi_{\mathbf{x}}(\gamma) = \begin{cases} 1, & \exists t \in [0, 1],\ \gamma(t) = \mathbf{x}, \\ 0, & \text{otherwise.} \end{cases} \tag{12}$$

The value $\chi_{\mathbf{x}}(\gamma)$ equals to 1 if the curve γ passes through the point $\mathbf{x}$, and 0 otherwise.

One can point that the voting score map $\mathcal{V}$ are derived from those geodesic curves $\mathcal{G}_j$ for $1 \leq j \leq J$, whose computation heavily relies on the set of end points and the geodesic metric used. Firstly, in the classical geodesic voting model, the set of the end points can be chosen either from the boundary of the image domain, by the prescribed edge points [41], or by an adaptive farthest point sampling scheme [42]. Secondly, the geodesic metric used in the existing geodesic voting models can be categorized as a Riemannian case which is dominated by the image gradient features [41].

III. A New Generalized Geodesic Voting Method

In this paper, we consider a new geodesic voting method which takes into account the anisotropic and asymmetric edge features for building the voting score map $\mathcal{V}$. For this purpose, we apply the Finsler geodesic model with the symmetric quadratic metric, see Section II-A, to construct the set Φ of geodesic curves $\mathcal{G}_j$. Furthermore, an adaptive cut is taken into

Algorithm 1: Geodesic Voting with Adaptive Cut

Input : A landmark point $\mathbf{z}$ inside the target region
Output: Segmentation contour.

1 Compute the adaptive cut $\mathcal{C}_{\mathbf{z}}$ as in Section III-A.
2 Construct the set A of farthest points as in Section III-C1.
3 Construct the set Φ_{AQ} of voting paths.
4 Compute the voting score map $\mathcal{V}$ via Eq. (20).

account for constructing simple closed contours by concatenation of two minimal paths corresponding to each endpoint. Both paths, linking an endpoint and a source point located at the adaptive cut, are derived from the asymmetric quadratic metrics in opposite directions. In addition, a landmark point $\mathbf{z} \in \mathbb{M}$ inside the target region is required to set up the generalized geodesic voting framework for efficient interactive segmentation. In Fig. 3 and Algorithm 1, we illustrate the overview of the generalized geodesic voting method. In the following, we introduce the details for each step.

A. Computation of the Adaptive Cut

The adaptive cut is generated by computing a minimal path connecting a landmark point $\mathbf{z}$ inside the target region to a point $\mathbf{x}$ belonging to the image boundary $\partial\mathbb{M}$ [38]. It is built based on the Cohen-Kimmel minimal path model where the metric in Eq. (1) is simplified as $\mathcal{F}_{\mathrm{Iso}}(\mathbf{x}, \mathbf{u}) = \psi(\mathbf{x})\|\mathbf{u}\|$. The potential function ψ is designed so that the obtained minimal path comes cross the target boundary only once. For that purpose, we suppose that ψ has high values around the image edges to force the minimal path to evolve along the homogeneous region. Thus one has

$$\psi(\mathbf{x}) = \exp\big(\tau g(\mathbf{x})\big) + \epsilon_1, \tag{13}$$

where τ and ϵ_1 are two positive constants, and g is the magnitude of the image gradient, see Eq. (24). The geodesic distance map $\mathcal{U}_{\mathbf{z}} : \mathbb{M} \to \mathbb{R}_0^+$ can be computed by solving the HJB equation (5) associated with metric $\mathcal{F}_{\mathrm{Iso}}$.

The endpoint $\mathbf{b} \in \partial\mathbb{M}$ of the target adaptive cut $\mathcal{C}_{\mathbf{z}}$ can be detected by finding a point of minimum distance value, i.e.

$$\mathbf{b} := \underset{\mathbf{x}\in\partial\mathbb{M}}{\arg\min}\, \mathcal{U}_{\mathbf{z}}(\mathbf{x}). \tag{14}$$

Finally, the adaptive cut $\mathcal{C}_{\mathbf{z}}$ is then can be generated using the solution to the gradient descent ODE (7) on $\mathcal{U}_{\mathbf{z}}$ such that $\mathcal{C}_{\mathbf{z}}(0) = \mathbf{p}$ and $\mathcal{C}_{\mathbf{z}}(1) = \mathbf{b}$. Since the adaptive cut is intersected with the target boundary only once, it is possible to track the minimal path from one side of the cut to the other side.

B. Asymmetry-enhanced Minimal Paths with Adaptive Cut

In this section, the asymmetric minimal paths are computed to depict the target boundary, benefiting from the edge asymmetry features and cut-convexity constraint introduced by the asymmetric quadratic metric and the adaptive cut, respectively.

From a source point to an endpoint located at the target edge, two anisotropic and asymmetric minimal paths can be traced along two opposite edge tangent directions based on the asymmetric quadratic metric, due to its edge asymmetry features carried out by the gradient vector ϖ (See Eq. (10)). Then a closed contour is attempt to be established by combination of these two minimal paths sharing the same source and target points in order to delineating the target boundary. For that purpose, the asymmetric quadratic metrics, constructed depending on different rotation matrix $\mathfrak{M}_i$ ($i \in \{0, 1\}$) involved by the vector field ω_i (See Eq. (11)) in the second part of the metric, are utilized to track minimal paths in counter-clockwise and clockwise directions. The corresponding asymmetric quadratic metrics read as

$$\mathcal{F}^0_{\mathrm{AQ}}(\mathbf{x}, \mathbf{u}) = \sqrt{\langle \mathbf{u}, \mathcal{M}(\mathbf{x})\mathbf{u}\rangle + \langle \omega_0(\mathbf{x}), \mathbf{u}\rangle_+^2}, \tag{15}$$

$$\mathcal{F}^1_{\mathrm{AQ}}(\mathbf{x}, \mathbf{u}) = \sqrt{\langle \mathbf{u}, \mathcal{M}(\mathbf{x})\mathbf{u}\rangle + \langle \omega_1(\mathbf{x}), \mathbf{u}\rangle_+^2}. \tag{16}$$

In contrast to the isotropic metric which is independent to the path tangents, it is possible for the asymmetric quadratic metrics to generate different minimal paths with the identical source point and endpoint, done by reversing the vector field component. We show such an example in Fig. 4a, where the two minimal paths are respectively tracked by the metrics defined in Eqs. (15) and (16). However, it may fail to generate effective closed contours, especially when the source and target points are close to each other, since such situation improves the risk of shortcuts problem usually suffered by the minimal path model. It requires appropriate user-provided endpoints to describe the target correctly, limiting its applications in practice, see Figs. 4b and 4d for examples. In order to solve the issue, the adaptive cut [38] is introduced into the segmentation framework in connection with the minimal path model associated to the asymmetric quadratic metric. The use of the adaptive cut can avoid the shortcut problem by preventing the minimal paths from crossing the adaptive cut. Moreover, by the adaptive cut one can track two minimal paths linking the two sides of the cut and an endpoint, as shown in Figs. 4c and 4e where the two minimal paths can well delineate the target boundary.

The source point $\mathbf{s}$, which is at the adaptive cut and used for defining minimal paths, can be derived from the intersection point between the target boundary and the adaptive cut. In practice, the point $\mathbf{s}$ has the maximal magnitude of image gradients among all points in the adaptive cut. Then two minimal paths $\mathcal{G}_0$ and $\mathcal{G}_1$, associated with asymmetric quadratic metrics $\mathcal{F}^0_{\mathrm{AQ}}$ and $\mathcal{F}^1_{\mathrm{AQ}}$, can be tracked along two sides of the adaptive cut from the source point to the endpoint, respectively.

In the remaining part of this section, we present the computation of the minimal path $\mathcal{G}_1$ from $\mathbf{s}$ (at the left side of the adaptive cut) to $\mathbf{e}$ as an example. The geodesic distance map $\mathcal{U}_1$ can be estimated by HFM [36]. In the course of the geodesic distance computation, the fast marching fronts propagation advances from the source point $\mathbf{s}$ and will not cross the cut, see Appendix A, and the procedure terminates when the end point $\mathbf{e}$ is reached. After the geodesic distance map is attained, the minimal path can be tracked by solving the ODE (7). The path $\mathcal{G}_0$ that travels from the left side of the adaptive cut and links from $\mathbf{s}$ to the endpoint $\mathbf{e}$ is tracked by the same way with $\mathcal{G}_1$.

C. Principle for the Introduced Geodesic Voting Model

In order to achieve reliable and robust segmentation in various situations. We extend the Riemannian metric based voting model to a Finsler case, which takes into account both the edge anisotropy and asymmetry features for image segmentation, depending on a collection of anisotropic and asymmetric minimal paths.

1) Building the Set of Endpoints: In this work, we make use of the farthest point sampling (FPS) scheme [42] to generate a set of points $A = \{\mathbf{p}_k \in \mathbb{M}; 1 \leq k \leq N\}$ with $N \geq 3$, by which we build the set of endpoints for computing the anisotropic and asymmetric minimal paths.

All points in the adaptive cut $\mathcal{C}_{\mathbf{z}}$ are utilized as model initialization to search for the farthest points [42]. Note that these points in $\mathcal{C}_{\mathbf{z}}$ will not be taken as the sampled farthest points. We denote by $\mathcal{P}$ as the set of the sampled farthest points. At the first iteration step, we set $\mathcal{P} : \mathcal{P}^{(0)} = \mathcal{C}_{\mathbf{z}}$, where we denote by $\mathcal{P}^k$ the updated set $\mathcal{P}$ at the k-th iteration. The first farthest point $\mathbf{p}_1$ can be detected via the corresponding geodesic distance map $\mathcal{U}_{\mathcal{C}_{\mathbf{z}}}$ with $\mathcal{P} = \mathcal{P}^{(0)}$ as

$$\mathbf{p}_1 = \arg\max_{\mathbf{x}\in\mathbb{M}} \mathcal{U}_{\mathcal{P}}(\mathbf{x}).$$

Note that the map $\mathcal{U}_{\mathcal{P}}$ is the solution to a HJB equation with isotropic metric of potential $\exp(\lambda g(\mathbf{x}))$, where $\lambda \in \mathbb{R}^+$ is a weighting parameter and g is defined in Eq. (24). Then one updates $\mathcal{P}$ as $\mathcal{P}^{(1)} = \mathcal{P}^{(0} \cup \{\mathbf{p}_1\}$. In the k-th $(1 < k \leq N)$ iteration procedure, the k-th farthest point $\mathbf{p}_k$ is detected by

$$\mathbf{p}_k = \arg\max_{\mathbf{x}\in\mathbb{M}} \mathcal{U}_{\mathcal{P}}(\mathbf{x}).$$

This yields the updated set $\mathcal{P}^{(k)} = \mathcal{P}^{(k-1)} \cup \{\mathbf{p}_k\}$. Finally, the farthest point set A can be generated as

$$A = \mathcal{P} \backslash \mathcal{C}.$$

In Fig. 3a, we illustrate examples for such endpoints on the images with the desired objects surrounded by complex background.

2) Geodesic Voting Method with Path Selection Criteria: By these endpoints, the set of minimal paths for constructing the voting score map can be established using asymmetric minimal paths connected to each endpoint involved in the farthest point set A, depending on the asymmetric quadratic metric defined in Section III-B. Figs. 3b and 3c illustrate the minimal paths associated with the asymmetric quadratic metrics. Note that all minimal paths are emanated from the source point as the interaction point between the target boundary and the adaptive cut. Let $\Phi_{\text{AQ}} = \{\mathcal{G}_{i,j}\}_{1\leq i\leq N}^{j\in\{0,1\}} \subset \text{Lip}([0,1],\mathbb{M})$ denote the set of voting paths, where N is the total number of endpoints. For each endpoint $\mathbf{p}_i \in A$, two minimal paths $\mathcal{G}_{i,0}$ and $\mathcal{G}_{i,1}$ associated to the metrics $\mathfrak{F}^0_{\text{AQ}}$ in Eq. (15) and $\mathfrak{F}^1_{\text{AQ}}$ in Eq. (16) are computed from the initial point $\mathbf{s}$ along two sides of the adaptive cut, respectively. The geodesic distance maps denoted as $\mathcal{U}_{i,0}$ and $\mathcal{U}_{i,1}$ are estimated by the adapted Hamiltonian fast marching (HFM) method in conjunction with the adaptive tut, as described in Appendix A, meanwhile the geodesic flows $\mathbf{V}_{i,0}$ and $\mathbf{V}_{i,1}$ can be derived from the corresponding distance maps as defined in Eq. (6).

(a) (b)

Fig. 5. Examples of the selected paths used for computing the voting score map. **a** The solid line is the chosen voting path with lower weighted curve length. **b** The cyan dot is the endpoint which leads to two minimal paths whose tangents (arrows) at the endpoint satisfy Eq. (18).

Path competition procedure for the voting score map. For each endpoint $\mathbf{p}_i \in A$, only the minimal path $\mathcal{G}_{i,j}$ with lower weighted curve length is chosen for voting score construction, which has a high possibility to depict the target boundary in practice. For an endpoint $\mathbf{p}_i$, one can obtain two minimal paths $\mathcal{G}_{i,0}$ and $\mathcal{G}_{i,1}$ with respect to two geodesic distance maps $\mathcal{U}_{i,0}$ and $\mathcal{U}_{i,1}$. In this case, the weighted lengths of $\mathcal{G}_{i,0}$ and $\mathcal{G}_{i,1}$ are $\mathcal{U}_{i,0}(\mathbf{p}_i)$ and $\mathcal{U}_{i,1}(\mathbf{p}_i)$. Then we denote by $\hat{\mathcal{G}}_i$ the path with lower length between $\mathcal{G}_{i,0}$ and $\mathcal{G}_{i,1}$, i.e. $\hat{\mathcal{G}}_i = \mathcal{G}_{i,0}$ if $\mathcal{U}_{i,0}(\mathbf{p}_i) < \mathcal{U}_{i,1}(\mathbf{p}_i)$, and $\hat{\mathcal{G}}_i = \mathcal{G}_{i,1}$, otherwise. For convenience, we define

$$\Phi_{\mathcal{D}} = \left\{\hat{\mathcal{G}}_i\right\}_{1\leq i\leq N}.$$

The voting score map $\mathcal{V}^{\mathcal{D}} : \mathbb{M} \to [0,\infty)$ associated to the initial point $\mathbf{s}$ is defined as

$$\mathcal{V}^{\mathcal{D}}(\mathbf{x}) = \sum_{\mathcal{G}\in\Phi_{\mathcal{D}}} \chi_{\mathbf{x}}(\mathcal{G}), \tag{17}$$

where $\chi_{\mathbf{x}}$ is a path detector defined in Eq. (12). However, the obtained voting score map $\mathcal{V}^{\mathcal{D}}$ may miss some part of the target boundary in complex scenarios, especially where the boundary is blurred. In Fig. 5a, we show an example for the path competition procedure, where the solid line is the chosen voting path.

Closed paths procedure for the voting score map. In this section, we are devoted to constructing the voting score map based on the closed minimal paths those delineate the target boundary. Recall that the closed path for each endpoint $\mathbf{p}_i$ is generated by tracing two anisotropic and asymmetric minimal paths from the adaptive cut as described in Section III-B. However, the shortcuts problem may occur when the endpoint is far away from the target boundary or close to the source point, leading to the minimal path does not evolve along the target boundary.

For each pair of minimal paths $\mathcal{G}_{i,0}$ and $\mathcal{G}_{i,1}$ to $\mathbf{p}_i \in A$, they are considered to form a closed contour that depicts the complete target, if the geodesic flows at the endpoint are inverse to each other. The Euclidean scalar product of the

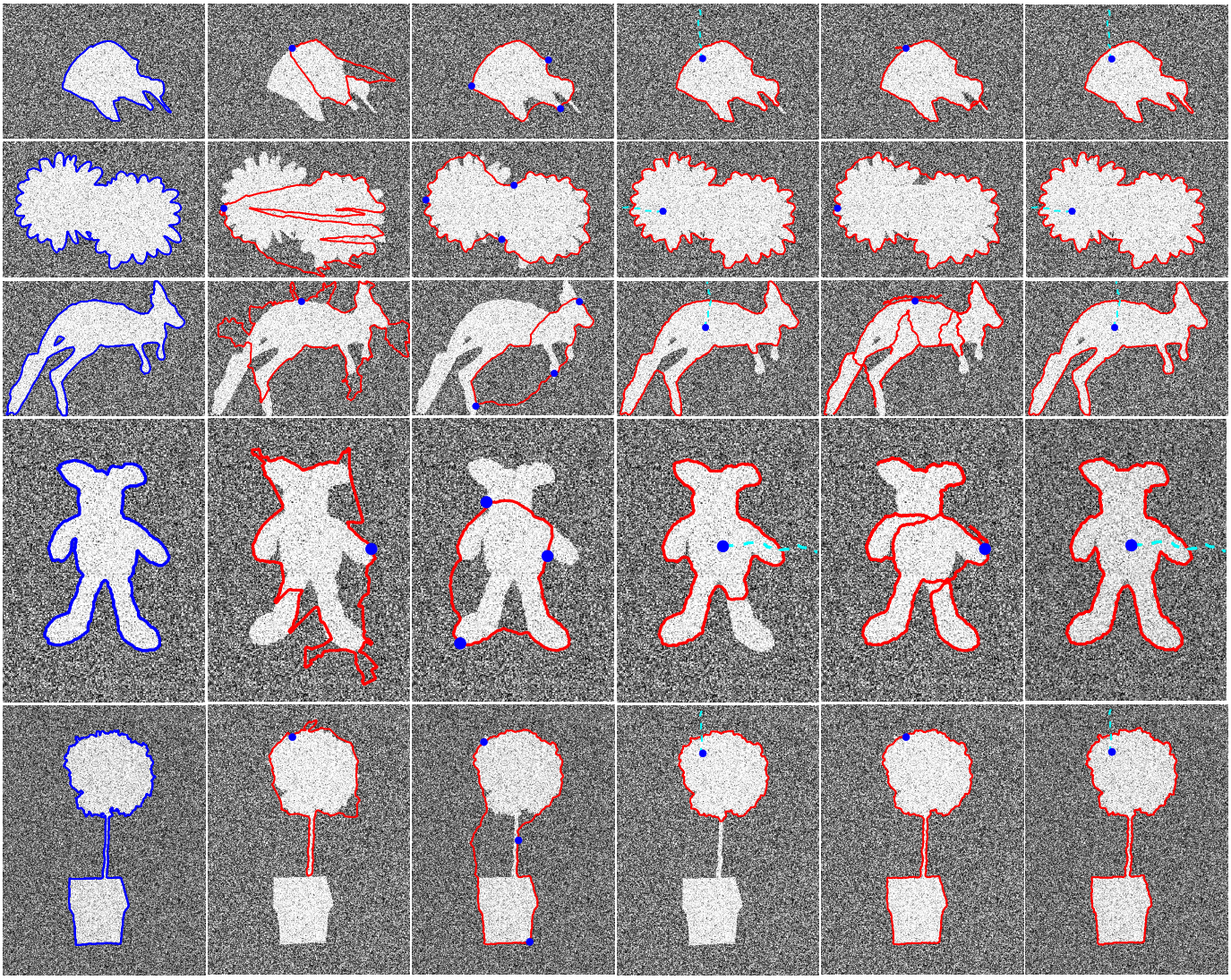

Fig. 6. Segmentation results on synthetic images interrupted by additive Gaussian noise with normalized standard derivation $\sigma_n = 0.15$. The red lines represent the segmentation contours and the landmark points are denoted by blue dots. The blue dash lines stand for the ground truth. The green dotted lines denote the cuts. **Column 1**: The original synthetic images. **Columns 2-6**: The segmented results detected by the AnisoVS model [15], the ComPaths model [17], the Asy-adapt model [16], the AsyVS model, the AsyVS-adapt model, respectively.

vector fields at point $\mathbf{p}_i$, derived from the geodesic flow maps $\mathbf{V}_{i,0}$ and $\mathbf{V}_{i,1}$, is expressed as

$$\mathcal{T}(\mathbf{p}_i) = \frac{\langle \mathbf{V}_{i,0}(\mathbf{p}_i), \mathbf{V}_{i,1}(\mathbf{p}_i) \rangle}{\|\mathbf{V}_{i,0}(\mathbf{p}_i)\| \|\mathbf{V}_{i,1}(\mathbf{p}_i)\|}, \tag{18}$$

with $\mathcal{G}_{i,0}(1) = \mathcal{G}_{i,1}(1) = \mathbf{p}_i$. Given a threshold $\zeta \in [-1, 0)$, the minimal paths $\mathcal{G}_{i,0}$ and $\mathcal{G}_{i,1}$ linked to $\mathbf{p}_i$ is regarded as the selected closed path if $\mathcal{T}(\mathbf{p}_i) < \zeta$. An instance of a pair of minimal paths satisfying the condition is illustrated in Fig. 5b. The corresponding geodesic flows at the endpoint, denoted by magenta and green arrows, are inverse to each other. In this work, we set $\zeta = -0.9$ for the experiments.

We denote by $\Phi_{\mathcal{F}} = \{\mathcal{G}_{n,j}\}_{1 \leq n \leq M, 0 \leq j \leq 1}$ a set involving all minimal paths satisfying the above condition from Φ_{AQ}, where $M \in (0, N]$ is a positive integer denoting the number of the selected minimal paths. Then, the second voting score map $\mathcal{V}^{\mathcal{F}} : \mathbb{M} \to [0, \infty)$ can be established as

$$\mathcal{V}^{\mathcal{F}}(\mathbf{x}) = \sum_{\mathcal{G} \in \Phi_{\mathcal{F}}} \chi_{\mathbf{x}}(\mathcal{G}). \tag{19}$$

At last, the final voting score map $\mathcal{V} : \mathbb{M} \to [0, \infty)$ associated to the initial point $\mathbf{s}$ is defined as

$$\mathcal{V}(\mathbf{x}) = \alpha \mathcal{V}^{\mathcal{F}}(\mathbf{x}) + \beta \mathcal{V}^{\mathcal{D}}(\mathbf{x}), \tag{20}$$

where the weight parameters α and β are used to control the importance of the two voting score maps. Examples of the voting score maps are shown in Fig. 3d.

3) Final Segmentation: In the voting score map, a strong value of $\mathcal{V}(\mathbf{x})$ indicates a high possibility that $\mathbf{x}$ belongs to the target boundary. A thresholding procedure is then applied to the voting score map $\mathcal{V}$ to obtained the segmentation results. Furthermore, mathematical morphological operators are used to refine the segmentation results to get contours whose

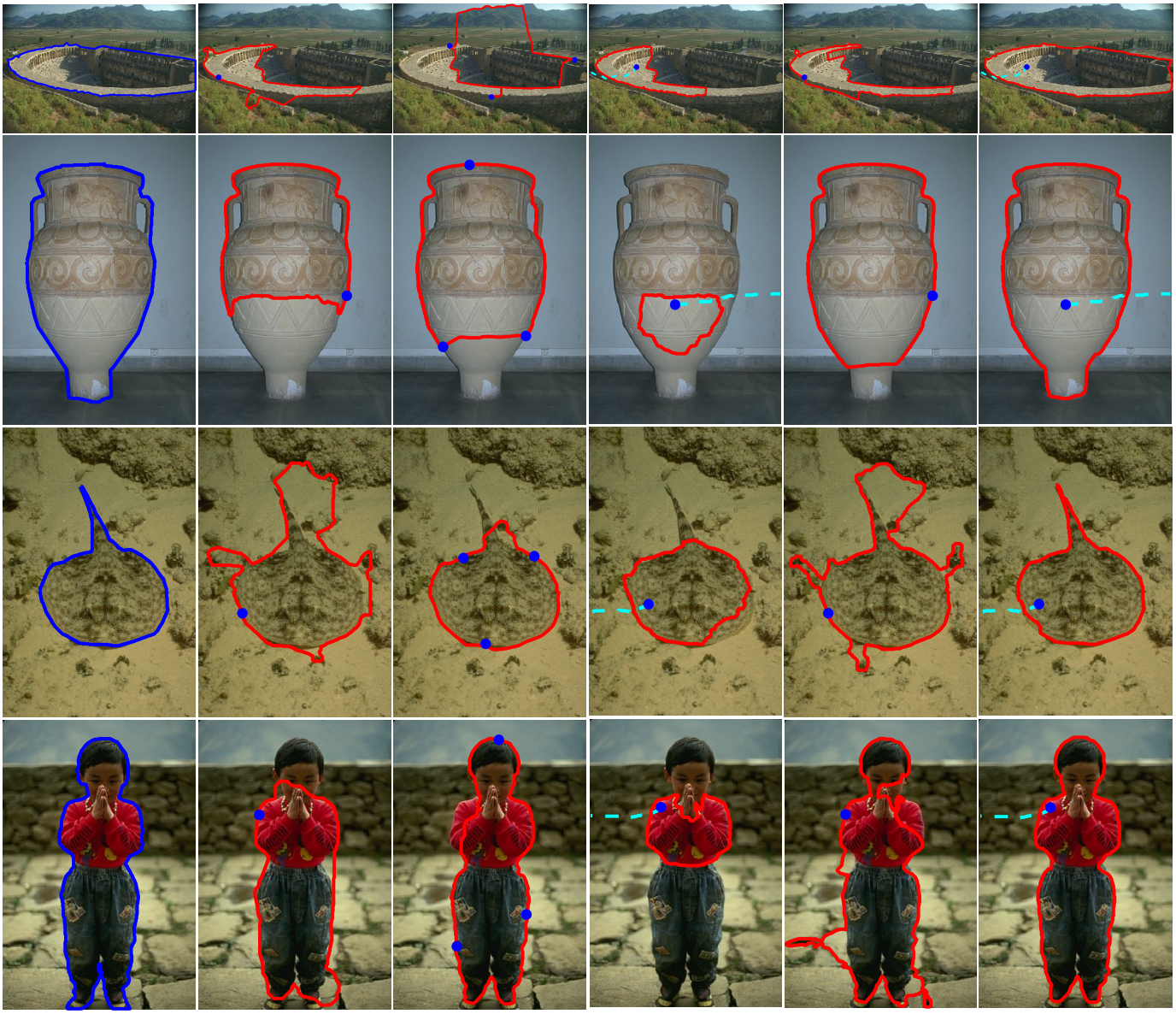

Fig. 7. Qualitative comparison results on nature images. The red lines represent the segmentation contours and the landmark points are denoted by blue dots. The blue dash lines stand for the ground truth. The green dotted lines denote the cuts. **Column 1**: The original CT images. **Columns 2-6**: The segmented results detected by the AnisoVS model [15], the ComPaths model [17], the Asy-adapt model [16], the AsyVS model, the AsyVS-adapt model, respectively.

width is single grid point. We illustrate the final segmentation contour in Fig. 3f.

IV. Experiments

We conduct the numerical experiments with both qualitative and quantitative comparison to the combination of piecewise-geodesic paths (ComPaths) model [17], the anisotropic Riemannian metric based geodesic voting segmentation (AnisoVS) model [15], the dual-cut model [16] with a spatial asymmetric quadratic metric (AsyMetric), the asymmetric quadratic metric based geodesic voting segmentation (AysVS) model and the proposed model (AysVS-adapt).

A. Parameter Setting and Initialization for the Tested Models

In the proposed model, a random landmark point inside the target region is required to start the segmentation procedure. The adaptive cut is computed from the landmark point based on the isotropic minimal path model, in the potential function (13) of which we set the parameters as $\tau = 1$ and $\epsilon_1 = 0.1$. Then the set of endpoints is built on farthest point sampling scheme from the adaptive cut and we set the number of endpoints as $N = 1000$. In the next, the minimal path models are tracked based on the asymmetric quadratic metric, and we set $a_2 = -6$ in Eq. (9) and $\lambda = 2$ in Eq. (11). In the final voting score map defined in Eq. (20), both parameters α and β are set as 1. In the last step, the thresholding value is set as 100 to get the final segmentation contours. For the ComPaths model [17], a closed contour is detected by concentrating a set of user-provided points using piecewise-geodesic paths. We provide three points on the target boundary as the initial points. In the AsyMetric

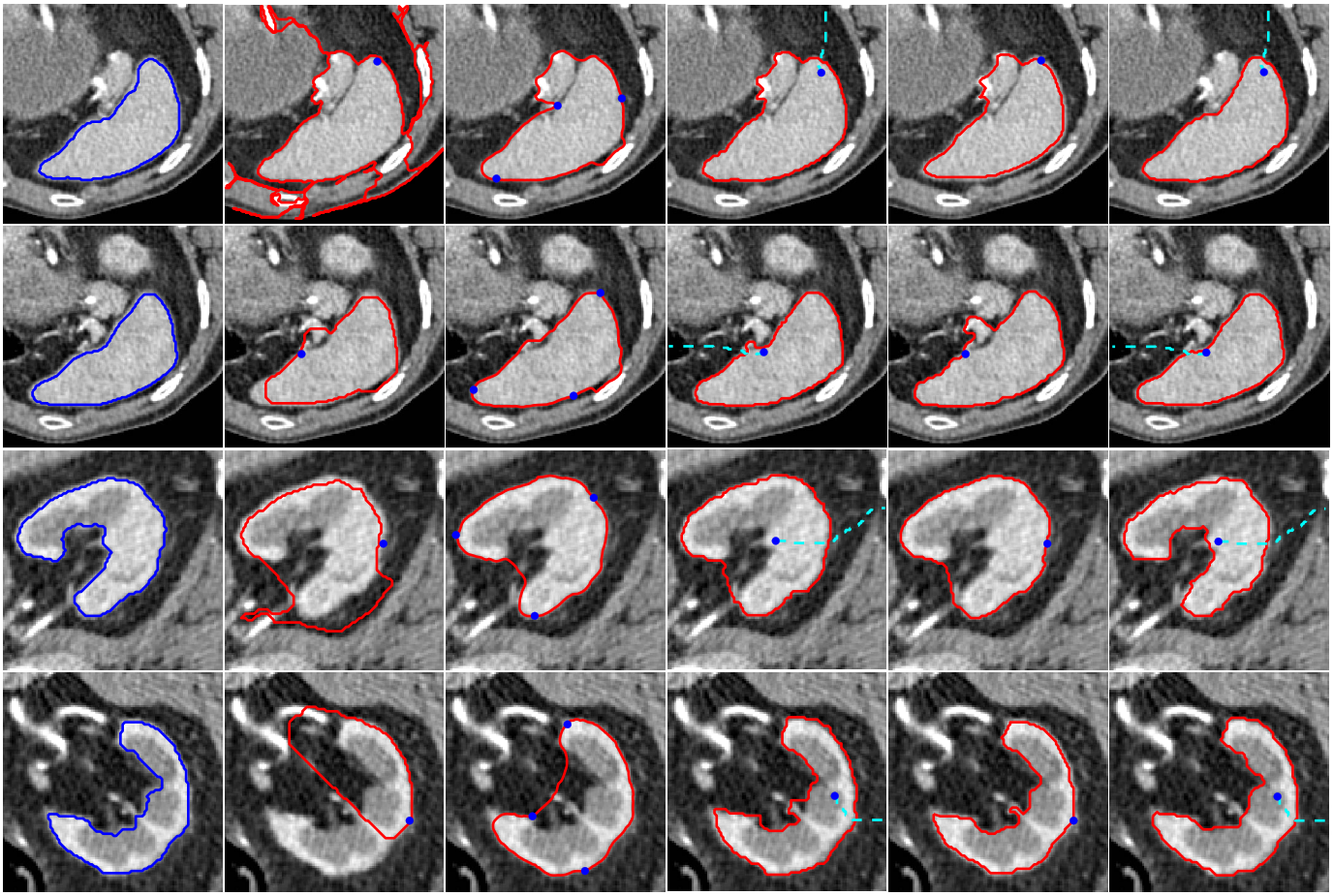

Fig. 8. Qualitative comparison results on CT images. The red lines represent the segmentation contours and the landmark points are denoted by blue dots. The blue dash lines stand for the ground truth. The green dotted lines denote the cuts. **Column 1**: The original CT images. **Columns 2-6**: The segmented results detected by the AnisoVS model [15], the ComPaths model [17], the Asy-adapt model [16], the AsyVS model, the AsyVS-adapt model, respectively.

model [16], we make use of the adaptive cut instead of the dual-cut scheme in [16] and the model is referred as Aysadapt. In the AnisoVS model [15], the anisotropic Riemannian metric is obtained based on the tensor filed in Eq. (9). In the following experiment, the same set of endpoints are used for the voting score map based segmentation methods including the AnisoVS model the AysVS model and the AysVS-adapt model. Furthermore, the source point for each VS model to find minimal paths is the intersection point between the adaptive cut and the target boundary, which can be detected in the proposed model.

B. Qualitative Comparison Results

Firstly, we illustrate in Fig. 6 the qualitative comparison results on 5 synthetic images with additive Gaussian noise of normalized standard deviation $\sigma_n = 0.15$. These synthetic images, derived from the ground truth data of the dataset [43], are created by respectively setting the intensity values of the target structures and the background region as 1 and 0.5. In this case, the directions of the image gradients estimated from these images exhibit strong local homogeneity, i.e. the gradient vectors are uniformly point outside the target region. Fig. 6a shows the synthetic images where the blue lines indicate the expected segmentation contours. The user-provided landmark points are represented by blue dots. The adaptive cut is denoted as the cyan dotted line. The segmented results are shown as red lines. Columns 2 to 6 illustrate the segmentation results of different models. One can see that the AnisoVS, ComPaths, Asy-adapt and AsyVS models cannot detect the correct contours, due to the influence from the strong noise. Specifically, the AsyVS model without considering the adaptive cut may miss some parts of the target boundary. Finally, we can get that the proposed model extracts the region of interest successfully, benefitting from the use of an adaptive cut scheme and the asymmetric edge features. In contrast, the proposed model (AsyVS-adapt) indeed is able to find the satisfactory segmentation results.

In Fig. 7, we show the qualitatively comparison results of different models on nature images [44]. The target objects surrounded by complicated background have complex shapes and intensity inhomogeneity. Besides, some target boundaries are not clearly. The segmented results from different models are depicted as red lines in columns 2 to 6 of Fig. 7. The adaptive cut is shown as cyan dotted lines. We can get that the classic models fail to track the correct boundary where the intensity inhomogeneity exists or the edge appearance features are weak, meanwhile the proposed model is able to detect the

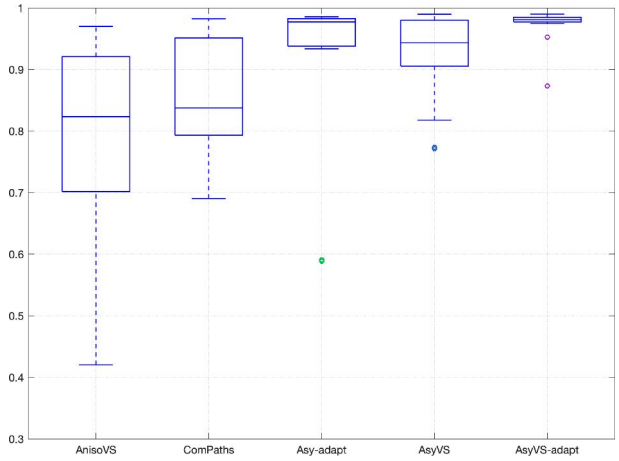

Fig. 9. Box plots of the average Dice scores $\mathcal{J}$ of 10 runs per image over all synthetic images for different methods.

target boundaries correctly.

Fig. 8 demonstrates the qualitative comparison results on CT images. The ground truth segmentation contours are indicated as blue lines as in column 1. The segmentation results are shown in columns 2 to 6. For the results from the AnisoVS, ComPaths, Asy-adapt and AsyVS models, either segmentation leakage or segmentation shortcut problems are observed along the blurred edges or when the target object has similar intensities with the neighboring regions. One can see that the proposed model shown in column 6 indeed can accurately delineate the target boundaries.

C. Quantitative Comparison Results

For evaluating the proposed model in a rigorous and convincing manner, here we run the quantitative comparisons. The accuracy that measures the performance of the tested models is carried out by a score $\mathcal{J}$ defined as follows:

$$\mathcal{J} = \frac{\#|S \cap GT|}{\#|S|}, \tag{21}$$

where S is the set of grid points passed through by the evaluated paths, GT denotes the region of the ground truth, and $\#|S|$ stands for the elements involved in the set S. The accuracy score $\mathcal{J}$ is ranged within the interval $[0, 1]$, where higher values of $\mathcal{J}$ means better performance.

In order to compare the robustness of different models with respect to different noise levels, we evaluate different models on the synthetic images shown in Fig. 6. In this experiment, each test image is generated by adding to the corresponding binary images different levels of additive Gaussian noise, whose normalized standard derivation values range from $\sigma_n = 0.03$ to 0.15 of scale 0.05. This yields 25 synthetic images for this comparison experiments. Note that the used 5 synthetic images with noise level $\sigma_n = 0.15$ are shown in column 1 of Fig. 6. Furthermore, the experiment is also carried out on these synthetic images to test the robustness of the models to different initializations. For the Asy-adapt and proposed models, 10 landmark points are randomly selected within the target region of each synthetic image to initialize the models. Then the adaptive cut can be tracked from each landmark point to the boundary of image domain. The source point is detected as the point which has maximal gradient magnitude along the adaptive cut. For the AnisoVS and AsyVS model, we choose 10 landmark points distributed along the target boundary of each synthetic image for the initialization. The landmark point is regarded the source point for minimal paths tracking in the voting score map construction. For the ComPaths model, 10 groups of sampled points are established on each synthetic image for initialization. For each group, three points are detected along the target boundary. Therefore, 10 tests per synthetic image are performed for all compared models, and the average of the Dice segmentation accuracy index for each image is computed from all tested models. The results are shown in Fig. 9. We can conclude that similar segmentation results from the proposed model are achieved with respect to different landmark points, which means that the proposed model is robust to the position of initialization. The average and standard deviation values of the Dice index with respect to different levels of noises are depicted in Table I. It can be observed that the proposed model is more robust against different levels of noise.

In order to quantitatively evaluate the segmentation accuracy of the proposed model, we perform the quantitative comparison for different models on 86 CT images [45]. This is implemented by utilizing a same procedure with the experiments on synthetic images to generate the initialization for the comparison models. In this case, 10 runnings per CT image are carried out with respect to each tested model. The quantitative comparison results are illustrated in Table II. In this experiment, we add the evaluation result of a deep learning based approach [46] which is referred to as the *segment anything (SA) model*. In these test CT images as shown in Fig. 8, the target boundaries often appear as weak edges, or suffer from strong influence from neighbouring regions. Due to the use of the asymmetric metrics and the new geodesic voting scheme, the proposed model the achieves the best accuracy performance among all the comparable models. Moreover, the SA model which uses the sampled landmark points as its prompt indeed obtains lower accuracy performance then the ComPaths, Asy-adpt AsyVS and the introduced AsyVS-adapt models, due to the lack of geometric regularization.

D. Computation Complexity

The computational complexity of the proposed geodesic voting method mainly consists of three parts: (i) the computation of the adaptive cut, (ii) the construction of the farthest points and (iii) the computation of the voting paths. Let $\mathcal{N}$ be the total number of grid points in $\mathbb{M}_h$. Specifically, the computation of the adaptive cut is implemented via the classical fast marching method, whose complexity is $\mathcal{O}(\mathcal{N} \ln \mathcal{N})$. As in [42], the complexity for the construction of the set of farthest points are lower than $\mathcal{O}(\mathcal{N} \ln(\mathcal{N})^2)$. Finally, the computation of the voting paths is implemented via the HFM method, which invokes a wide neighborhood system dependent to the metrics. The computation complexity of the HFM is $\mathcal{O}(2\mathcal{N}(\mathcal{K}+\ln \mathcal{N}))$, where $\mathcal{K}$ is the average size of the local neighbourhood of

TABLE I
THE QUANTITATIVE COMPARISON RESULTS OF THE ANISOVS, COMPATHS, ASY-ADAPT, ASYVS, AND ASYVS-ADAPT MODELS ON SYNTHETIC IMAGES.

Noise Level	AnisoVS		ComPaths		Asy-adapt		AsyVS		AsyVS-adapt	
	Mean	Std	Mean	Std	Mean	Std	Mean	Std	Mean	Std
0.03	0.9387	0.0487	0.8948	0.1161	0.9037	0.1855	0.9813	0.0201	**0.9828**	**0.0049**
0.06	0.9125	0.0786	0.8814	0.1207	0.9025	0.1860	0.9637	0.0527	**0.9816**	**0.0056**
0.09	0.7903	0.1364	0.8461	0.1606	0.8970	0.1836	0.9348	0.0949	**0.9801**	**0.0054**
0.12	0.7084	0.1897	0.8503	0.1381	0.8927	0.1825	0.8805	0.1139	**0.9611**	**0.1383**
0.15	0.6143	0.1942	0.8047	0.1736	0.8869	0.1811	0.8711	0.1199	**0.9754**	**0.0146**

TABLE II
THE QUANTITATIVE COMPARISON RESULTS OF THE SA MODEL, THE ANISOVS MODEL, THE COMPATHS MODEL, THE ASY-ADAPT MODEL, THE ASYVS MODEL, AND THE ASYVS-ADAPT MODEL ON A SET OF CT IMAGES.

SA		AnisoVS		ComPaths		Asy-adapt		AsyVS		AsyVS-adapt	
Mean	Std	Mean	Std	Mean	Std	Mean	Std	Mean	Std	Mean	Std
0.86134	0.15447	0.7368	0.1458	0.8741	0.0948	0.8960	0.1207	0.9296	0.0889	**0.9555**	**0.0220**

all grid points. Finally, we point out that the computation time on the CPU-implemented HFM method can be greatly reduced via a GUP-implemented parallel computing method as proposed in [47].

We report the computation time of the proposed model evaluated on the set of CT images. The average computation time is around 5.93s per image, where the farthest point sampling costs 4.97s per image with 1000 sampled points. The experiments are performed on a standard 8-core Intel Core i7 of 3.8GHz architecture with 64Gb RAM.

E. Limitations and Future Work

In this section, we discuss the limitations of the introduced geodesic voting method. Firstly, the computation of voting paths only relies on the image gradient features, but independent to the image region-based homogeneity features and curvature regularization. Secondly, it requires a user-provided point to initialize the proposed geodesic voting model. The future work will be devoted to addressing the issues above: (i) combining with the region-based Randers minimal path model [19] to the generate a new method for computing voting paths, and (ii) using the deep learning-based segmentation approaches to predict the initialization of the proposed model.

V. CONCLUSION

In this paper, we show the possibility of implementing the geodesic voting method for image segmentation task. A crucial step is to generate simple closed contour by combining the adaptive cut and the minimal path model with asymmetric quadratic metrics. Accordingly, the proposed interactive segmentation model enables to blend the benefits from the disconnection constraint on the image domain and the image edge anisotropic and asymmetric features. This approach is adapted to automatically segment complex objects by only providing a landmark point randomly inside the target region. The experimental results prove that the proposed models indeed outperform other methods described in the literature.

ACKNOWLEDGMENT

The authors thank the editors and all the reviewers for their invaluable time to read and evaluate this manuscript. This work is in part supported by the National Natural Science Foundation of China (NOs. 62102210, 62172243), the Shandong Provincial Natural Science Foundation (NOs. ZR2021QF029, ZR2022YQ64), projects in QLUT (2023RCKY253).

APPENDIX A
NUMERICAL SOLUTIONS

The HJB equation (5) associated to an asymmetric quadratic metric can be efficiently solved using the fast marching methods [13], [36], [37], [48], [49] in a single-pass wavefronts propagation manner. The numerical solution to (5), denoted by $U : \mathbb{M}_h \to [0, \infty)$, is defined in a discretization orthogonal grid $\mathbb{M}_h := \mathbb{M} \cap \mathbb{Z}^d$, where h is the grid scale. In the course of the geodesic distance computation U, the fast marching front is expanded from the source point $\mathbf{s}$ and visits each point $\mathbf{x} \in \mathbb{M}_h$ monotonically, with initialization $U(\mathbf{s}) = 0$.

As in [38], we adapt the Hamiltonian fast marching (HFM) method [36] to estimate the geodesic distance map U on the grid $\mathbb{M}_h$ in conjunction with an adaptive cut. The core of the HFM lies at the approximation of the Hamiltonian $\mathcal{H}_{\mathbf{x}}$ using positively-valued weights $\{\rho_j(\mathbf{x})\}_{1\leq j\leq J}$ and offsets $\{\dot{\mathbf{e}}_j(\mathbf{x})\}_{1\leq j\leq J}$ whose coordinates are integers

$$\mathcal{H}_{\mathbf{x}}(\mathbf{v}) \approx \sum_{1\leq i\leq I} \rho_i(\mathbf{x}) \langle \mathbf{v}, \dot{\mathbf{e}}_i(\mathbf{x}) \rangle_+^2 \tag{22}$$

where $\langle \mathbf{v}, \dot{\mathbf{e}}_i(\mathbf{x})\rangle_+^2 = \max\{0, \langle \mathbf{v}, \dot{\mathbf{e}}_i(\mathbf{x})\rangle\}^2$. By the approximation (22), then the HJB equation (5) can be discretized to the form

$$\sum_{1\le j\le J} \rho_j(\mathbf{x}) \max\{0, U(\mathbf{x}) - U(\mathbf{x} - h\dot{\mathbf{e}}_j(\mathbf{x}))\}^2 = h^2.$$

Note that all the offsets $\dot{\mathbf{e}}_j(\mathbf{x})$ at each grid point $\mathbf{x}$ determine the neighbourhood system, i.e. the points $(\mathbf{x} - h\dot{\mathbf{e}}_j) \in \mathbb{M}_h$ for $1 \le j \le J$ are the neighbor points of $\mathbf{x}$. When an adaptive cut $\mathcal{C}$ is taken into account, we need to refine the neighbourhood system by removing some offsets or equivalently setting the corresponding weight to 0, i.e. for any index $1 \le j \le J$

$$\rho_j(\mathbf{x}) = 0, \quad \mathcal{C} \cap [\mathbf{x}, \mathbf{x} - h\dot{\mathbf{e}}_j(\mathbf{x})] \neq \emptyset,$$

where $[\mathbf{x}, \mathbf{x} - h\dot{\mathbf{e}}_j]$ denotes the straight segment between $\mathbf{x}$ and $\mathbf{x} - h\dot{\mathbf{e}}_j(\mathbf{x})$ We refer to [38] for more details on the computation of geodesic distances in the presence of an adaptive cut.

APPENDIX B
IMAGE GRADIENT FEATURES

The edge-based features of images are usually extracted based on the image gradients. The gradients can be computed by building a Jacobian matrix [50]. For a gray level image $I : \mathbb{M} \to \mathbb{R}$, the image gradient can be expressed as

$$J_\sigma(\mathbf{x}) = (\partial_x G_\sigma * I, \partial_y G_\sigma * I)^T(\mathbf{x}),$$

where ∂_x and ∂_y denote the first-order partial derivative along x- and y-axis directions of the Gaussian kernel G_σ with variance σ, and " $*$ " represents the convolution operator. In addition, the gradients of a color image $\mathbf{I} = (I_1, I_2, I_3)$ in a RGB color space can be described as

$$J_\sigma(\mathbf{x}) = \begin{pmatrix} \partial_x G_\sigma * I_1, & \partial_x G_\sigma * I_2, & \partial_x G_\sigma * I_3 \\ \partial_y G_\sigma * I_1, & \partial_y G_\sigma * I_2, & \partial_y G_\sigma * I_3 \end{pmatrix}(\mathbf{x}).$$

Then the edge appearance features can be estimated by computing the gradient magnitude as the Frobenius norms of the matrix $J(\mathbf{x})$, reading as

$$\tilde{g}(\mathbf{x}) = \sqrt{\sum_{k=1}^{n} \Big(\|(\partial_x G_\sigma * I_k)(\mathbf{x})\|^2 + \|(\partial_y G_\sigma * I_k)(\mathbf{x})\|^2 \Big)}, \tag{23}$$

where the parameter n is belonging to $[1, 3]$, $n = 1$ for the gray level image and $n = 3$ for the color image, and $\|\cdot\|$ denotes the Euclidean norm. In practice, the magnitudes $\tilde{g}$ is normalized to the appearance feature by

$$g(\mathbf{x}) = \frac{\tilde{g}(\mathbf{x})}{\|\tilde{g}\|_\infty}, \quad \forall \mathbf{x} \in \Omega. \tag{24}$$

With the definition, a strong value of $g(\mathbf{x})$ indicates that a high possibility that the point $\mathbf{x}$ locates at edge region.

Let $\mathbb{S}_2^+$ denote a set collecting all the positive definite symmetric matrices with size of 2×2. The edge anisotropic features for gray level and color images can be estimated by building a tensor filed $\mathcal{W} \in \mathbb{S}_2^+$ encoding anisotropic features, as following

$$\mathcal{W}(\mathbf{x}) = J_\sigma(\mathbf{x}) J_\sigma(\mathbf{x})^T + \epsilon \mathbf{I}_d \tag{25}$$

where $\mathbf{I}_d$ denotes the identity with size of 2×2 and the parameter ϵ is a sufficiently small positive constant to avoid singularity.

REFERENCES

[1] M. Kass, A. Witkin, and D. Terzopoulos, "Snakes: Active contour models," *Int. J. Comput. Vis.*, vol. 1, no. 4, pp. 321–331, 1988.

[2] Zhaobin Wang, Baozhen Ma, and Ying Zhu, "Review of level set in image segmentation," *Archives of Computational Methods in Engineering*, vol. 28, pp. 2429–2446, 2021.

[3] J. Zhang, Z. Lu, and M. Li, "Active contour-based method for finger-vein image segmentation," *IEEE Trans. Instrum. Meas.*, vol. 69, no. 11, pp. 8656–8665, 2020.

[4] A. Niaz, E. Iqbal, A. A. Memon, A. Munir, J. Kim, and K. N. Choi, "Edge-based local and global energy active contour model driven by signed pressure force for image segmentation," *IEEE Trans. Instrum. Meas.*, vol. 72, pp. 1–14, 2023.

[5] M. Monemian and H. Rabbani, "Analysis of a novel segmentation algorithm for optical coherence tomography images based on pixels intensity correlations," *IEEE Trans. Instrum. Meas.*, vol. 70, pp. 1–12, 2020.

[6] V. Caselles, R. Kimmel, and G. Sapiro, "Geodesic active contours," *Int. J. Comput. Vis.*, vol. 22, no. 1, pp. 61–79, 1997.

[7] J. Melonakos, E. Pichon, S. Angenent, and A. Tannenbaum, "Finsler active contours," *IEEE Trans. Pattern Anal. Mach. Intell.*, vol. 30, no. 3, pp. 412–423, 2008.

[8] S. Osher and J. A. Sethian, "Fronts propagating with curvature-dependent speed: algorithms based on hamilton-jacobi formulations," *J. Comput. Phys.*, vol. 79, no. 1, pp. 12–49, 1988.

[9] T. F. Chan, B. Y. Sandberg, and L. A. Vese, "Active contours without edges for vector-valued images," *J. Vis. Commun. Image Represent.*, vol. 11, no. 2, pp. 130–141, 2000.

[10] C. Li, C. Kao, J. C. Gore, and Z. Ding, "Minimization of region-scalable fitting energy for image segmentation," *IEEE Trans. Image Process.*, vol. 17, no. 10, pp. 1940–1949, 2008.

[11] G. Wang, F. Zhang, Y. Chen, G. Weng, and H. Chen, "An active contour model based on local pre-piecewise fitting bias corrections for fast and accurate segmentation," *IEEE Trans. Instrum. Meas.*, vol. 72, pp. 1–13, 2023.

[12] L. D. Cohen and R. Kimmel, "Global minimum for active contour models: A minimal path approach," *Int. J. Comput. Vis.*, vol. 24, no. 1, pp. 57–78, 1997.

[13] J. A. Sethian, "Fast marching methods," *SIAM Review*, vol. 41, no. 2, pp. 199–235, 1999.

[14] J.-M. Mirebeau and J. Portegies, "Hamiltonian fast marching: a numerical solver for anisotropic and non-holonomic eikonal PDEs," *Image Processing On Line*, vol. 9, pp. 47–93, 2019.

[15] Vijaya K. Ghorpade and Laurent D. Cohen, "Automatic image segmentation with anisotropic fast marching algorithm and geodesic voting," in *2015 IEEE International Conference on Image Processing (ICIP)*, 2015, pp. 3009–3013.

[16] D. Chen, J. Zhu, X. Zhang, M. Shu, and L. D. Cohen, "Geodesic paths for image segmentation with implicit region-based homogeneity enhancement," *IEEE Trans. Image Process.*, vol. 30, pp. 5138–5153, 2021.

[17] J. Mille, S. Bougleux, and L. D. Cohen, "Combination of piecewise-geodesic paths for interactive segmentation," *Int. J. Comput. Vis.*, vol. 112, no. 1, pp. 1–22, 2015.

[18] B. Appleton and H. Talbot, "Globally optimal geodesic active contours," *J. Math. Imaging Vis.*, vol. 23, no. 1, pp. 67–86, 2005.

[19] D. Chen, J.-M. Mirebeau, H. Shu, and L. D. Cohen, "A Region-based Randers geodesic approach for image segmentation," *Int. J. Comput. Vis.*, vol. 132, no. 2, pp. 349–391, 2024.

[20] D. Chen, J.-M. Mirebeau, and L. D. Cohen, "Global minimum for a Finsler elastica minimal path approach," *Int. J. Comput. Vis.*, vol. 122, no. 3, pp. 458–483, 2017.

[21] R. Duits, S. PL Meesters, J.-M. Mirebeau, and J. M Portegies, "Optimal paths for variants of the 2d and 3d reeds–shepp car with applications in image analysis," *J. Math. Imag. Vis.*, vol. 60, no. 6, pp. 816–848, 2018.

[22] D. Chen, J.-M. Mirebeau, M. Shu, and L. D. Cohen, "Computing geodesic paths encoding a curvature prior for curvilinear structure tracking," *Proc. Nat. Acad. Sci.*, vol. 120, no. 33, pp. e2218869120, 2023.

[23] Chen D., Mirebeau J.-M., Shu M., Tai X.-C., and Cohen L. D., "Geodesic models with convexity shape prior," *IEEE Trans. Pattern Anal. Mach. Intell.*, vol. 45, no. 7, pp. 8433–8452, 2023.

[24] Y. Rouchdy and L. D. Cohen, "Geodesic voting for the automatic extraction of tree structures. methods and applications," *Comput. Vis. Image Understand.*, vol. 117, no. 10, pp. 1453–1467, 2013.

[25] Maria A Zuluaga, Maciej Orkisz, Pei Dong, Alexandra Pacureanu, Pierre-Jean Gouttenoire, and Françoise Peyrin, "Bone canalicular network segmentation in 3d nano-ct images through geodesic voting and image tessellation," *Physics in Medicine & Biology*, vol. 59, no. 9, pp. 2155, 2014.

[26] Shervin Minaee, Yuri Boykov, Fatih Porikli, Antonio Plaza, Nasser Kehtarnavaz, and Demetri Terzopoulos, "Image segmentation using deep learning: A survey," *IEEE transactions on pattern analysis and machine intelligence*, vol. 44, no. 7, pp. 3523–3542, 2021.

[27] Thorsten Falk, Dominic Mai, Robert Bensch, Özgün Çiçek, Ahmed Abdulkadir, Yassine Marrakchi, Anton Böhm, Jan Deubner, Zoe Jäckel, Katharina Seiwald, et al., "U-net: deep learning for cell counting, detection, and morphometry," *Nature methods*, vol. 16, no. 1, pp. 67–70, 2019.

[28] Hu Cao, Zhongnan Qu, Guang Chen, Xinyi Li, Lothar Thiele, and Alois Knoll, "GhostViT: Expediting Vision Transformers Via Cheap Operations," *IEEE Transactions on Artificial Intelligence*, 2023.

[29] Jiacai Liao, Libo Cao, Wei Li, Yang Ou, Cong Duan, and Hu Cao, "Fully-supervised semantic segmentation networks: Exploring the relationship between the segmentation networks learning ability and the number of convolutional layers," in *2021 7th International Conference on Computer and Communications (ICCC)*. IEEE, 2021, pp. 1685–1692.

[30] Hu Cao, Yueyue Wang, Joy Chen, Dongsheng Jiang, Xiaopeng Zhang, Qi Tian, and Manning Wang, "Swin-unet: Unet-like pure transformer for medical image segmentation," in *Proc. ECCV*. Springer, 2022, pp. 205–218.

[31] Maciej A Mazurowski, Haoyu Dong, Hanxue Gu, Jichen Yang, Nicholas Konz, and Yixin Zhang, "Segment anything model for medical image analysis: an experimental study," *Medical Image Analysis*, vol. 89, pp. 102918, 2023.

[32] Jun Ma, Yuting He, Feifei Li, Lin Han, Chenyu You, and Bo Wang, "Segment anything in medical images," *Nature Communications*, vol. 15, no. 1, pp. 654, 2024.

[33] Ziwei Liu, Xiaoxiao Li, Ping Luo, Chen-Change Loy, and Xiaoou Tang, "Semantic image segmentation via deep parsing network," in *Proc. ICCV*, 2015, pp. 1377–1385.

[34] Ping Luo, Guangrun Wang, Liang Lin, and Xiaogang Wang, "Deep dual learning for semantic image segmentation," in *Proc. ICCV*, 2017, pp. 2718–2726.

[35] Yaochi Zhao, Shiguang Liu, and Zhuhua Hu, "Focal learning on stranger for imbalanced image segmentation," *IET Image Processing*, vol. 16, no. 5, pp. 1305–1323, 2022.

[36] J.-M. Mirebeau, "Riemannian fast-marching on Cartesian grids, using Voronoi's first reduction of quadratic forms," *SIAM J. Numer. Anal.*, vol. 57, no. 6, pp. 2608–2655, 2019.

[37] J.-M. Mirebeau, "Fast-marching methods for curvature penalized shortest paths," *J. Math. Imag. Vis.*, vol. 60, no. 6, pp. 784–815, 2018.

[38] Li Liu, Da Chen, Minglei Shu, and Laurent D. Cohen, "Grouping boundary proposals for fast interactive image segmentation," *IEEE Transactions on Image Processing*, vol. 33, pp. 793–808, 2024.

[39] G. Randers, "On an asymmetrical metric in the four-space of general relativity," *Phys. Rev.*, vol. 59, no. 2, pp. 195, 1941.

[40] D. Chen, J. Spencer, J.-M. Mirebeau, K. Chen, M. Shu, and L. D. Cohen, "A generalized asymmetric dual-front model for active contours and image segmentation," *IEEE Trans. Image Process.*, vol. 30, pp. 5056–5071, 2021.

[41] V. K. Ghorpade and L. D. Cohen, "Automatic image segmentation with Anisotropic Fast Marching algorithm and geodesic voting," in *Proc. ICIP*. IEEE, 2015, pp. 3009–3013.

[42] G. Peyré and L. D. Cohen, "Geodesic remeshing using front propagation," *Int. J. Comput. Vis.*, vol. 69, no. 1, pp. 145–156, 2006.

[43] C. Rother, V. Kolmogorov, and A. Blake, "Grabcut: Interactive foreground extraction using iterated graph cuts," *ACM Trans. Graph.*, vol. 23, no. 3, pp. 309–314, 2004.

[44] Pablo Arbeláez, Michael Maire, Charless Fowlkes, and Jitendra Malik, "Contour detection and hierarchical image segmentation," *IEEE Transactions on Pattern Analysis and Machine Intelligence*, vol. 33, no. 5, pp. 898–916, 2011.

[45] J. Spencer, K. Chen, and J. Duan, "Parameter-free selective segmentation with convex variational methods," *IEEE Trans. Image Process.*, vol. 28, no. 5, pp. 2163–2172, 2019.

[46] Alexander Kirillov, Eric Mintun, Nikhila Ravi, Hanzi Mao, Chloe Rolland, Laura Gustafson, Tete Xiao, Spencer Whitehead, Alexander C Berg, Wan-Yen Lo, et al., "Segment anything," in *Proc. ICCV*, 2023, pp. 4015–4026.

[47] J.-M. Mirebeau, L. Gayraud, R. Barrère, D. Chen, and F. Desquilbet, "Massively parallel computation of globally optimal shortest paths with curvature penalization," *Concurrency Computat., Pract. Exper.*, vol. 35, no. 2, pp. e7472, 2023.

[48] J.-M. Mirebeau, "Anisotropic fast-marching on cartesian grids using lattice basis reduction," *SIAM J. Numer. Anal.*, vol. 52, no. 4, pp. 1573–1599, 2014.

[49] J.-M. Mirebeau, "Efficient fast marching with Finsler metrics," *Numer. Math.*, vol. 126, no. 3, pp. 515–557, 2014.

[50] N. Sochen, R. Kimmel, and R. Malladi, "A general framework for low level vision," *IEEE Trans. Image Process.*, vol. 7, no. 3, pp. 310–318, 1998.